

A Fully Convolutional Approach to Denoising Structural Dynamics Data from X-Ray Photon Correlation Spectroscopy

Nisar Nellikunnummel*, Andi Barbour, Lutz Wiegart, Tatiana Konstantinova† and Anthony DeGennaro‡

Brookhaven National Laboratory, Upton, NY 11973, USA

May 29, 2026

Abstract

We present a fully convolutional denoising autoencoder (FC-DAE) for denoising two-time intensity-intensity correlation functions (C_2) in X-ray photon correlation spectroscopy (XPCS). Unlike conventional denoising autoencoders that are typically restricted to fixed input sizes, the FC-DAE accepts inputs of arbitrary dimensions while preserving correlation structures across diverse dynamical regimes. The model is trained using experimentally derived C_2 data collected at NSLS-II beamlines, with data augmentation applied to expand the diversity of the dataset and reduce overfitting. The FC-DAE successfully recovers intricate dynamical features in low signal-to-noise conditions while maintaining structural fidelity. To assess reconstruction reliability, we employ quantitative metrics to evaluate structural fidelity and identify potential model-induced bias. Our results demonstrate that the FC-DAE provides robust denoising performance with high computational efficiency, enabling recovery of XPCS dynamics under photon-limited and low-dose measurement conditions.

1 Introduction

X-ray photon correlation spectroscopy (XPCS) probes structural dynamics in materials by analyzing intensity fluctuations in coherent X-ray speckle patterns produced by the interference of X-rays scattered from randomly distributed inhomogeneities within the material [1]. This technique is well-suited for investigating both equilibrium and nonequilibrium dynamics across a wide range of systems. Specifically, XPCS is used to probe mesoscale dynamics in processes such as the aging of glasses [2], colloidal gelation [3], polymer relaxation [4], and the fluctuations of magnetic domains [5]. The two-time intensity-intensity correlation function, $C_2(q, t_1, t_2)$, is used to quantify the temporal evolution of intensity fluctuations in the scattered X-ray signal. It is defined as:

$$C_2(q, t_1, t_2) = \frac{\langle I(q, t_1)I(q, t_2) \rangle}{\langle I(q, t_1) \rangle \langle I(q, t_2) \rangle} \quad (1)$$

where $I(q, t)$ represents the scattered intensity at wave vector q and time t , and $\langle \rangle$ denotes an ensemble average, typically performed over a range of detector pixels at constant q . $C_2(q, t_1, t_2)$ is a two-dimensional matrix that quantifies the correlation between intensities at times t_1 and t_2 . The $C_2(q, t_1, t_2)$ matrix is symmetric about its main diagonal ($t_1 = t_2$), allowing the raw time coordinates t_1 and t_2 to be transformed into physically meaningful axes: the age axis, t_{age} , and the lag axis, τ [6]. The age axis represents the evolution of the system since the start of the measurement and is defined as the average of the two time points, $t_{\text{age}} = (t_1 + t_2)/2$. The lag axis represents the duration of the measured fluctuations and is defined

*nnellikun@bnl.gov

†Currently at: Amazon

‡Currently at: GE Aerospace Research

as the time difference, $\tau = |t_2 - t_1|$. In the limit of stationary dynamics, $C_2(q, t_1, t_2)$ reduces to the one-time correlation function, $g_2(q, \tau)$, by averaging $C_2(q, t_1, t_2)$ over the t_{age} axis at a constant τ .

$$g_2(q, \tau) = \langle C_2(q, t_1, t_2) \rangle_{t_{\text{age}}} \quad (2)$$

Henceforth, $C_2(q, t_1, t_2)$ is denoted as C_2 , and $g_2(q, \tau)$ as g_2 . The time variables t_1 , t_2 , t_{age} , and τ are discretized in units of detector frames, corresponding to uniformly sampled time intervals (lags) during XPCS measurements. Thus, all correlation functions are evaluated on a discrete time grid, where the frame index serves as a proxy for physical time (lag time) and can be converted to real time using the known frame acquisition rate.

The distinction between equilibrium and nonequilibrium dynamics lies in whether relaxation is time-invariant. In equilibrium, C_2 depends only on lag time, τ , leading to a constant relaxation rate and uniform correlation width along the age axis t_{age} in the C_2 . In contrast, nonequilibrium dynamics are non-stationary, with relaxation times evolving over t_{age} , appearing as broadening or narrowing of the correlation profile. They may also include stochastic events, such as avalanches or sudden structural rearrangements, which manifest as discrete breaks or discontinuous dynamics along t_{age} .

To interpret g_2 physically, it is related to the underlying dynamics through the Siegert relation [7]:

$$g_2 = C_\infty + \beta |g_1(q, \tau)|^2 \quad (3)$$

where C_∞ denotes the baseline and $\beta_0 = \beta + C_\alpha - 1$ ($0 < \beta_0 \leq 1$) is the instrumental coherence factor, or contrast. The normalized intermediate scattering function, $g_1(q, \tau)$, encodes the sample dynamics, with different functional forms corresponding to different relaxation behaviors. Consequently, the measured g_2 is fitted to models appropriate for the dynamics under study. In nonequilibrium systems, where the dynamics evolve with t_{age} , this relation is applied locally within quasi-stationary regions of the data.

In practice, nonequilibrium XPCS analysis often requires slicing C_2 along the age axis t_{age} to obtain locally stationary regions suitable for fitting. For noisy data, adjacent slices are typically averaged over an age window Δt_{age} to achieve sufficient signal-to-noise ratio (SNR) for reliable parameter extraction. This approach implicitly assumes that the dynamics remain approximately stationary within Δt_{age} ; however, when this condition is not satisfied, the averaging process reduces temporal resolution and can introduce bias in the extracted parameters. Furthermore, selecting an appropriate binning window often requires expert judgment and becomes increasingly impractical for large datasets.

These challenges are further compounded by the inherently noisy nature of experimental C_2 data. In practice, the dominant limitations arise not only from detector imperfections but, more fundamentally, from photon-limited measurement conditions. As a result, effective denoising methods are essential for improving data quality and enabling reliable extraction of dynamical information. The primary challenges and the role of denoising in addressing them are summarized as follows:

- **Photon-limited conditions:** Limited coherent flux reduces the number of detected photons per frame, such that increasing temporal resolution or probing larger q (smaller length scales) leads to reduced SNR. Denoising enables recovery of meaningful correlation signals under these conditions.
- **Low-dose measurements:** Radiation-sensitive samples often require reduced X-ray exposure to mitigate beam damage, which further degrades SNR. Denoising allows reliable extraction of dynamics while operating at lower dose.
- **Detector artifacts:** Occasional detector-related events, such as hot pixels, can introduce temporally correlated artifacts in C_2 (e.g., streaks along rows and columns). Denoising helps suppress these distortions and improves overall data fidelity.

Conventional denoising methods, such as Gaussian and mean filtering [8,9], suppress noise by averaging neighboring values, often blurring fine correlation features essential for accurate dynamical analysis. Denoising Autoencoders (DAEs) [10–12] offer a promising solution by learning the functional form of the dynamic signal obscured by noisy data, enabling effective denoising while preserving the intrinsic dynamics. However, a key limitation of DAEs is their reliance on a fixed latent space, which requires inputs of a fixed size and restricts the model’s flexibility when handling arbitrarily sized data. Additionally, the use of a fixed

latent representation introduces significant bias, even when the latent space is relatively large. While DAEs can effectively denoise complex patterns present in the training domain, they face a significant challenge in generalization. Because the latent space of a DAE is shaped by the dynamics represented in the training data [12], the model may struggle to generalize to qualitatively different correlation patterns. This highlights two major demerits of the DAE approach: first, the necessity for massive, high-fidelity datasets to populate the latent space; and second, the difficulty of training a single ‘universal’ model. Instead, DAEs often require specialized models tailored to specific classes of dynamics, as any signal not explicitly captured during the large-scale training phase is likely to be misinterpreted as noise and suppressed.

To overcome these limitations, we propose a Fully Convolutional Denoising Autoencoder (FC-DAE) based on a Fully Convolutional Network architecture [13]. By eliminating fully connected layers, the FC-DAE can process C_2 s of arbitrary spatial dimensions, making it directly applicable to experimental XPCS datasets without the need for resizing or cropping. More importantly, the model preserves physically meaningful structures in noisy data and can capture complex oscillatory or intermittent features beyond dynamics well described by the standard Kohlrausch–Williams–Watts (KWW) [14] function. In addition to the architectural advancement, we introduce a set of quantitative reliability metrics to assess the fidelity and applicability of the denoised outputs, addressing the critical need to evaluate model-induced bias in scientific analysis. Fig. 1 illustrates representative cases where the latent-space DAE fails to recover underlying correlation features, either by over-smoothing or distorting the signal, while the FC-DAE retains these structures with significantly improved clarity. In this work, we demonstrate the effectiveness of the proposed approach using experimental XPCS datasets spanning a wide range of dynamical regimes, and show that it enables more reliable extraction of dynamic parameters from noisy measurements.

2 Dataset Preparation and Preprocessing

2.1 Experimental Dataset

Model training is conducted using data collected at the Coherent Hard X-ray Scattering (CHX) and Coherent Soft X-ray Scattering (CSX) beamlines of NSLS-II. In order for the model to denoise experimental data exhibiting a wide range of dynamical behaviors, the training dataset includes diverse C_2 patterns collected from XPCS experiments. Representative examples of such C_2 patterns are shown in Fig. 1. Many of these patterns are not adequately handled by previous DAE models [10, 11]. We used data from 119 unique experiments and selected several regions of interest in reciprocal space for each experiment when calculating C_2 . In total, 779 C_2 patterns were used for training, 56 for testing, and 58 for validation. The size of the C_2 patterns ranges from 134 to 2995 frames. Unlike previous DAE models trained primarily on datasets describable by KWW dynamics within individual Δt_{age} bins, our training dataset includes a broader range of complex and non-KWW-like dynamical behaviors.

2.2 Target Generation and Preprocessing

Generating experimental ground-truth pairs (noisy, noise-free) across a broad range of dynamics, timescales, and noise conditions is often unfeasible. To address this, we employ the DAE architecture of [11] as a target preparation model. We use raw C_2 ($C_{2,\text{raw}}$) as noisy inputs and the corresponding DAE outputs as proxy ‘noise-free’ targets, as illustrated by the top portion of Fig. 2. Although the DAE is not capable of accurately reconstructing large C_2 maps with complex nonstationary dynamics, its performance remains highly reliable when restricted to localized subregions (such as near-diagonal areas characterized by simpler, quasi-equilibrium dynamics). In our approach, we exploit this by using the DAE exclusively in these small subregions to generate stable, physically consistent surrogate targets for training. Importantly, the FC-DAE is not constrained by the limitations of the DAE. By utilizing a fully convolutional architecture, the model inherits a spatial invariance that forces local smoothing kernels to function uniformly across the entire map. Consequently, by training on targets that are already partially smoothed in reliable local regions, the FC-DAE learns robust denoising strategies that seamlessly generalize to larger scales and more complex global structures, ultimately outperforming its teacher model.

The DAE accepts only input data of a fixed size (100×100), and inputs are generated by cropping along the diagonal of the $C_{2,\text{raw}}$. A copy of each $C_{2,\text{raw}}$ with reversed t_{age} is also included to increase variability.

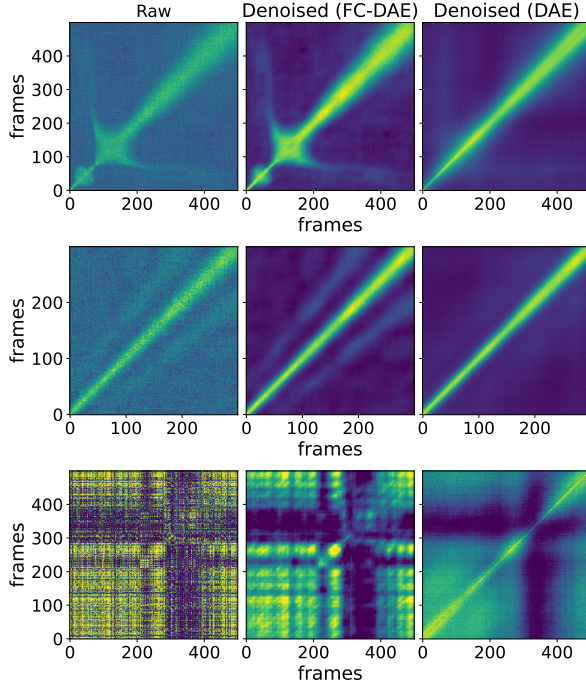


Figure 1: Representative examples of raw and denoised C_2 . The raw C_2 (left) is compared with denoised results from the FC-DAE (middle) and the conventional DAE (right). The FC-DAE successfully suppresses noise and preserves structural features where the DAE fails.

Additional data augmentation is performed by subsampling frames at different intervals—every 2nd, 3rd, 4th, 10th, 20th, and 30th frame—to generate new $C_{2,\text{raw}}$. The diagonal elements of $C_{2,\text{raw}}$ parallel to t_{age} represent trivial self-correlations dominated by photon counting statistics and instrumental noise rather than true dynamics. Therefore, prior to cropping, these values are replaced by the average of their nearest off-diagonal neighbors.

To assess robustness of model under varying signal-to-noise conditions, we generate bootstrapped $C_{2,\text{raw}}$ samples by randomly subsampling pixels within each frame prior to correlation calculation. Subsampling fractions of 50%, 25%, 10%, and 5% are used to systematically increase noise levels, producing multiple noisy realizations of the same underlying dynamics for validation with known, high fidelity ground truths.

Each input $C_{2,\text{raw}}$ is standardized to have zero mean and unit standard deviation before training. Standardizing the data ensures consistent feature scales for stable autoencoder training, enabling more effective noise removal by focusing the model on dynamic patterns rather than absolute signal magnitudes. Consequently, during model application, input data is first standardized. After the model generates the denoised output, the standardization is reversed to bring this output back to the original data’s scale.

3 FC-DAE Model Architecture

The model architecture is composed entirely of convolutional layers, structured into an encoder–decoder framework as illustrated in the lower portion of Fig 2. The encoder consists of five convolutional layers with 1, 4, 8, 16 and 32 output channels, respectively. The decoder mirrors this structure using transposed convolutional layers to reconstruct the denoised output. A kernel size of 3 is used consistently across all layers. Batch normalization is applied after each convolutional layer (or transposed convolutional) and before the activation function. The exponential linear unit (ELU) activation is used throughout the network, except in the final output layer, where no activation is applied. Strides of size 1 are used in each layer and the output of each layer is padded to preserve the spatial dimensions of the input.

We also investigated deeper variants of the encoder-decoder architecture by extending the five-layer

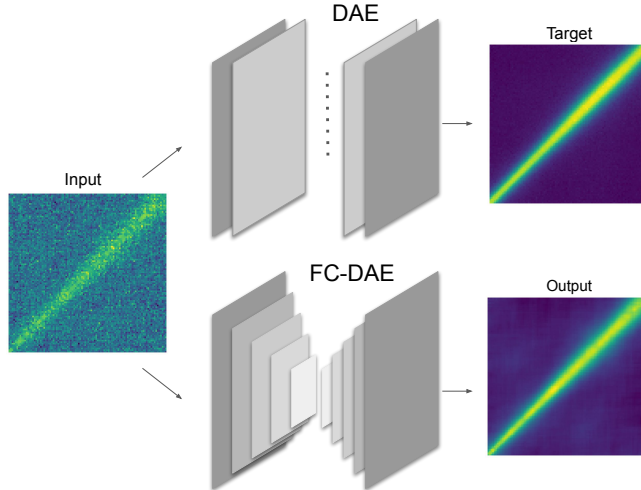


Figure 2: Architecture of a Fully Convolutional Denoising Autoencoder (FC-DAE) in a supervised training setup. The FC-DAE comprises multiple convolutional layers designed to denoise input images. During training, the output image is compared to a target (clean) image using a loss function, and the convolutional filters are optimized accordingly.

model to six and seven convolutional layers, introducing additional encoder layers with 64 and 128 output channels, respectively. While these deeper configurations significantly increased the number of trainable parameters and computational cost, no measurable improvement in denoising performance was observed compared with the baseline five-layer architecture. In addition, we explored the use of a larger convolutional kernel size of 5×5 in all layers to increase the effective receptive field. This modification likewise resulted in increased computational demand without yielding any noticeable performance gains. Consequently, the five-layer architecture with a 3×3 kernel was selected as the optimal trade-off between model complexity, computational efficiency, and denoising performance.

4 Training Strategy

The model learns convolutional filters tailored to the characteristics of the input data through supervised training. Training data preparation is described in Section. 2.2. The mean square error (MSE) between the output and the target is used as the training loss function. The convolutional kernel size controls the balance between capturing fine local details and broader contextual information, thereby influencing the trade-off between noise removal and detail preservation. To prevent overfitting, early stopping is applied during training when the loss function reaches a predefined threshold. Model optimization is performed using the Adam optimizer [15].

5 Model Variance

To quantify model uncertainty arising from random weight initialization, we estimated the variance of the FC-DAE using an ensemble approach. Ten independent models were trained with identical hyperparameters but different initialization seeds, ensuring distinct initial conditions while maintaining reproducibility. The validation set was used to assess the stability of the ensemble. For each validation sample, denoised outputs from the ten models were compared pixel-by-pixel across the $C_{2,\text{denoised}}$ maps to compute the ensemble variance, which was then averaged to obtain a single scalar variance per sample. Across all validation samples, the ensemble variance remained extremely low ($1.2\text{--}1.7 \times 10^{-4}$), indicating highly consistent predictions across different initializations. This demonstrates that the learned denoising mapping is stable and that uncertainty due to random initialization is negligible compared to the intrinsic noise in the raw inputs—a

result consistent with the reliable quantitative application of denoised C_2 s.

To assess the impact of model uncertainty on the extracted dynamics, we compared the ensemble variance of the autoencoder predictions with the corresponding observed contrast β_{obs} (estimated from the statistical distribution of the C_2 map using the 1st and 99th percentiles) for the validation sample. For each sample, ten independently initialized models were evaluated, and the pixel-wise variance across the ensemble was computed for each frame and averaged to obtain a single variance metric per sample, yielding an overall mean of $\langle \sigma_{\text{ens}}^2 \rangle = (1.457 \pm 0.016) \times 10^{-4}$. This is significantly lower than the observed mean contrast of $\langle \beta_{\text{obs}} \rangle = (1.84 \pm 0.12) \times 10^{-1}$. Consequently, the ratio $\sigma_{\text{ens}}^2 / \beta_{\text{obs}}$ typically falls on the order of 10^{-3} , with a median value of 1.0×10^{-3} and a 10–90 percentile range of $(4.6 \times 10^{-4}, 1.5 \times 10^{-3})$. These results demonstrate that the ensemble variance remains approximately three orders of magnitude smaller than β_{obs} , indicating that uncertainty due to random initialization has a negligible impact on the quantitative extraction of dynamical parameters.

6 Model Scope and Reliability Metrics

From a practical perspective, the primary source of uncertainty in the model arises from intrinsic bias introduced during denoising. Any denoising autoencoder must impose some bias to suppress noise while preserving meaningful structural information. Consequently, assessing the reliability of the denoised output requires evaluating how faithfully it represents the underlying sample dynamics. Although the FC-DAE is designed to handle a broad range of C_2 patterns, including complex dynamical behaviors, some cases cannot be reliably reconstructed. To address this, we introduce a set of quantitative metrics that evaluate different aspects of reconstruction reliability and determine whether the denoiser can be confidently applied to a given dataset. These metrics are evaluated on a validation set spanning a wide range of dynamical behaviors, including both well- and poorly reconstructed cases.

6.1 Relative Contrast Shift Analysis

To quantify the systematic bias introduced by FC-DAE, we evaluate the relative shift in observed contrast, defined as $\Delta\beta_{\text{obs, rel}} = (\beta_{\text{obs, denoised}} - \beta_{\text{obs, raw}}) / \beta_{\text{obs, raw}}$, where $\beta_{\text{obs, denoised}}$ represents the observed contrast after applying the denoising process and $\beta_{\text{obs, raw}}$ represents the original observed contrast prior to denoising. In XPCS, the speckle contrast is a fundamental physical parameter; therefore, a high-fidelity denoiser must preserve it without introducing artificial inflation or suppression.

Analysis of validation samples reveals that in high-contrast cases ($\beta_{\text{obs, raw}} > 0.1$), the model achieves high fidelity, with relative errors typically remaining below 5%. Conversely, significant bias ($\Delta\beta_{\text{obs, rel}} > 20\%$) is observed exclusively in low-signal regimes where $\beta_{\text{obs, raw}} < 0.05$. In these cases, the noise floor (measured as the standard deviation of the uncorrelated baseline) becomes comparable to the signal itself, leading the model to occasionally misidentify noise fluctuations as part of the physical correlation ridge. Overall, the relative contrast shift quantifies the robustness of FC-DAE across different C_2 signal regimes.

6.2 Residual Autocorrelation Analysis for Denoising Validation

To evaluate whether the FC-DAE effectively removes noise without distorting the underlying signal of the measured C_2 , we analyze the residual—defined as the difference between the raw and denoised signals: $C_{2, \text{denoised}} - C_{2, \text{raw}}$. Ideally, if the model captures all physically meaningful structures in the C_2 map, the residual should consist purely of uncorrelated noise. Any remaining structured pattern would indicate that the autoencoder failed to fully model the underlying correlation dynamics. To assess this, we compute a row-averaged autocorrelation function (ACF) of the residual matrix. For each row of the residual, the mean is first removed and the autocorrelation is calculated up to a specified maximum lag. The resulting ACFs from all rows are then averaged to obtain a mean residual ACF. If the residual is consistent with uncorrelated stochastic fluctuations, the autocorrelation values for all non-zero lags should fluctuate around zero and remain within the expected statistical confidence bounds. We therefore compare the averaged ACF against the theoretical confidence limit for the uncorrelated fluctuations, $\pm z / \sqrt{(N)}$, where N is the number of samples used to compute the autocorrelation for each row, and z corresponds to the confidence level of 95% ($z = 1.96$). When all non-zero lag values remain within this bound, the residual is considered statistically

indistinguishable from uncorrelated noise, indicating that no significant structured signal remains in the residual after denoising.

6.3 Structural Similarity Index

The Structural Similarity Index (SSIM) [16] is a widely used metric to compare two images based on luminance, contrast, and structural information, while emphasizing preservation of spatial features beyond simple pixel differences. The SSIM value ranges from -1 to 1 , where a value of 1 indicates identical images, values near zero indicate weak structural similarity, and negative values correspond to anticorrelated structures. SSIM provides a convenient way to assess how closely denoised C_2 reproduces the spatial patterns present in the raw data.

We computed the SSIM between $C_{2,\text{raw}}$ and the corresponding denoised $C_{2,\text{denoised}}$ for all samples in the validation dataset. The resulting SSIM values vary considerably in the validation dataset, indicating that FC-DAE reconstructs certain C_2 maps more reliably than others. Using a threshold of $\text{SSIM} \approx 0.15$ to distinguish meaningful structural recovery, about 24% of the validation samples can be classified as reliably reconstructed. It is important to note that a low SSIM value does not necessarily imply poor denoising performance. Since FC-DAE targets noise reduction, $C_{2,\text{denoised}}$ should not strictly replicate the original $C_{2,\text{raw}}$ pixels. In cases where $C_{2,\text{raw}}$ contains substantial noise, the removal of high-frequency fluctuations can reduce the apparent structural similarity between the two patterns. Therefore, SSIM should be interpreted primarily as an indicator of how well large-scale correlation patterns are preserved, rather than as a strict measure of denoising accuracy. For this reason, the SSIM analysis is complemented by additional diagnostics based on the statistical properties of the residual.

7 Extracting Dynamic Parameters

To evaluate the impact of denoising on quantitative analysis, we examine the extraction of dynamic parameters from the strongly oscillatory C_2 data shown in the top row of Fig. 3. The corresponding g_2 extracted from $C_{2,\text{raw}}$ is not well described by a single KWW function. Instead, we employ a composite model consisting of a KWW term and a damped sinusoidal component to capture the pronounced peaking behavior observed in g_2 . Both the raw and FC-DAE-denoised C_2 are sliced with a single-frame age window to obtain individual g_2 curves, and each slice is independently fitted to extract the dynamic parameters. Due to the limited lag time, slices at the extreme edges of the C_2 are excluded from fitting. Because the dynamics vary weakly along the diagonal of C_2 , we additionally collapse C_2 along the diagonal to form an ensemble-averaged g_2 , which serves as a reference for the mean behavior. As shown in the lower rows (b-e) of Fig. 3, the parameters extracted from the denoised C_2 exhibit substantially reduced uncertainties and are significantly closer to the ensemble-averaged values than those obtained from the raw data, demonstrating that FC-DAE enables reliable parameter extraction even in this complex dynamical regime. The bottom row of Fig. 3 displays the R^2 goodness-of-fit for each slice, demonstrating that the denoised data yields significantly better fits compared to the raw data.

8 Recovery of Dynamics in Photon-Limited Regimes

To assess the ability of the FC-DAE to recover meaningful dynamics from noisy inputs, we employ two complementary approaches. First, we performed a controlled degradation study using bootstrapped datasets C_2 as described in Section. 2.2 to systematically increase statistical noise. Second, we analyze C_2 obtained from regions of interest (ROIs) at increasing wavevector q , where reduced scattered intensity leads to lower SNR. Together, these approaches probe the robustness of the model across both synthetic and experimentally relevant noise conditions.

8.1 Recovery under Controlled Noise Degradation

Figure 4 illustrates the raw and FC-DAE-denoised C_2 maps together with the corresponding one-time correlation functions g_2 . We focus on the recovery of the oscillatory (peaking) component in g_2 , which is highly

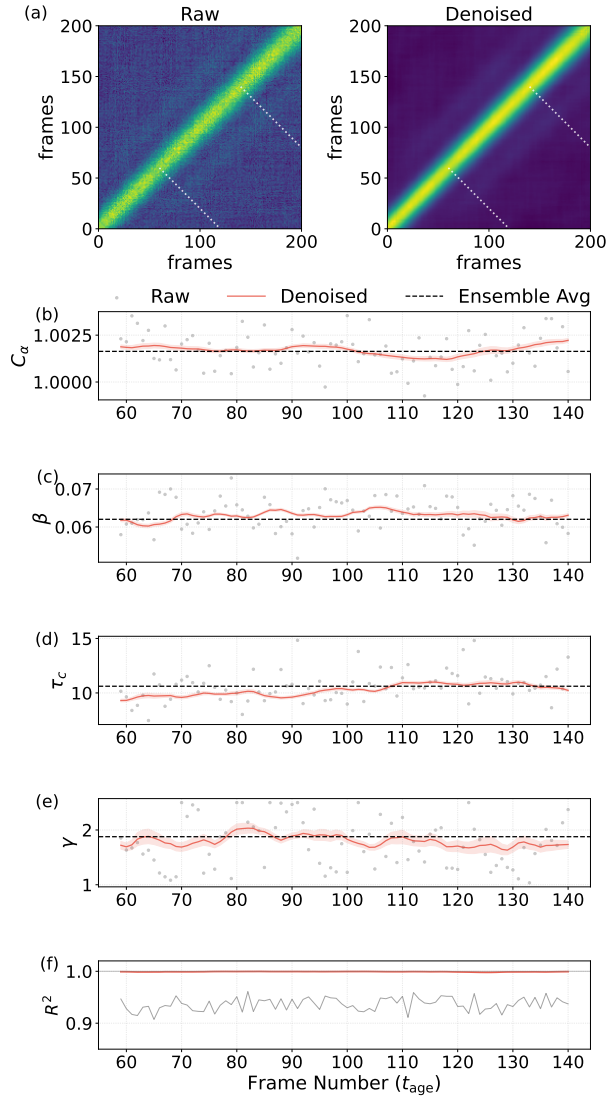


Figure 3: Comparison of correlation data and extracted dynamic parameters. (a) Representative raw (left) and FC-DAE-denoised (right) C_2 data. Slices within dotted lines are used for fitting. (b–e) Evolution of the four primary KWW parameters (C_α , β , τ_c , γ) as a function of frame number. The denoised results (red) exhibit substantially reduced statistical scatter compared to the raw slices (gray), while the ensemble average is shown as a dashed line. (f) The R^2 goodness-of-fit for each slice. Shaded regions represent the 1σ uncertainty derived from the fit covariance matrix.

sensitive to noise and therefore provides a stringent test of reconstruction fidelity. For moderate noise levels (50%, 25%, and 10% bootstrapping), the FC-DAE reliably reconstructs both the peak position and amplitude, yielding denoised g_2 curves that closely match the nominal behavior. At the most extreme degradation (5%), the peak is strongly suppressed in the raw data due to loss of statistical contrast, and the reconstructed signal correspondingly shows reduced amplitude, indicating the practical limit of recoverable information. These results demonstrate that the FC-DAE preserves nontrivial dynamical features over a wide range of noise levels while naturally reflecting information loss under severe undersampling.

8.2 Recovery across Wavevector-Dependent Noise Levels

To quantify reconstruction performance across experimentally relevant conditions, we analyze C_2 at increasing wavevectors q . As q increases, the scattered intensity per frame decreases, leading to progressively lower SNR. We consider C_2 datasets extracted from four regions of interest (ROIs) corresponding to consecutive q values, $q = 1, \dots, 4$. To quantify the SNR of C_2 , we adopt a definition tailored to XPCS data, where the one-time correlation function g_2 typically exhibits a stretched-exponential decay rather than a well-defined peak. We estimate the SNR from an off-diagonal of the C_2 corresponding to a fixed lag time τ , chosen such that the contrast decays to β_0/e , where β_0 is the initial contrast and e is Euler’s number. This ensures that the SNR is evaluated in a region where the signal remains meaningful while avoiding trivial self-correlations. The SNR is then computed as

$$\text{SNR} = \log_{10} \left(\frac{\langle \mathcal{D}_\tau \rangle}{\text{Var}(\mathcal{D}_\tau)} \right), \quad (4)$$

where $\mathcal{D}_\tau = \{C_2(t_{\text{age}}, t_{\text{age}} + \tau) \mid t_{\text{age}}\}$ denote the set of values along this diagonal, i.e., at constant τ and varying age t_{age} . The $\langle \mathcal{D}_\tau \rangle$ and $\text{Var}(\mathcal{D}_\tau)$ denote the mean and variance of the values along the selected diagonal.

Figure 5 summarizes the results. As shown in Fig. 5(a), the SNR of g_2 extracted from $C_{2,\text{raw}}$ decreases with increasing q , while the FC-DAE significantly restores the correlation signal. Notably, the denoised C_2 at $q = 4$ achieves an SNR comparable to that of the raw C_2 at $q = 1$, despite substantially reduced photon statistics. Based on the average ROI intensities at $q = 1$ and $q = 4$, these results suggest that FC-DAE denoising could enable XPCS measurements of faster dynamics by increasing the achievable frame rate by a factor of ~ 4.4 , or equivalently allow measurements to be performed using only $\sim 23\%$ of the original dose while maintaining comparable SNR. This interpretation is further supported by the diagonal analysis at constant τ time shown in Fig. 5(b). Fig. 5(c) presents the average ROI intensities for $q = 1$ and $q = 4$, confirming that measurements at higher q are performed under significantly lower intensity conditions.

These results demonstrate that the FC-DAE effectively compensates for reduced counting statistics, enabling reliable recovery of correlation signals at lower intensities. Consequently, denoising allows XPCS measurements to be performed at reduced flux or dose while maintaining comparable SNR, thereby extending the accessible experimental parameter space.

9 Conclusions

The proposed fully convolutional FC-DAE model provides robust denoising across a broad range of XPCS dynamics. Unlike latent-space DAE architectures, which require fixed-size inputs and highly specialized training domains, the FC-DAE can process C_2 inputs of arbitrary dimensions while generalizing across diverse dynamics and noise conditions. This enhanced generalizability is fundamentally driven by the spatial invariance of the fully convolutional architecture; by utilizing localized smoothing kernels rather than coordinate-dependent fully connected layers, the network naturally scales the denoising strategies learned from local subregions across the entire correlation map. Visual and quantitative comparisons show that the FC-DAE preserves physically meaningful correlation structures more effectively than conventional DAE approaches, particularly for complex nonequilibrium dynamics where latent-space models tend to oversmooth or distort the signal. To assess reconstruction fidelity, reliability metrics are incorporated to identify cases where the denoised output may deviate from physically meaningful behavior, particularly for previously unseen or highly complex dynamical regimes.

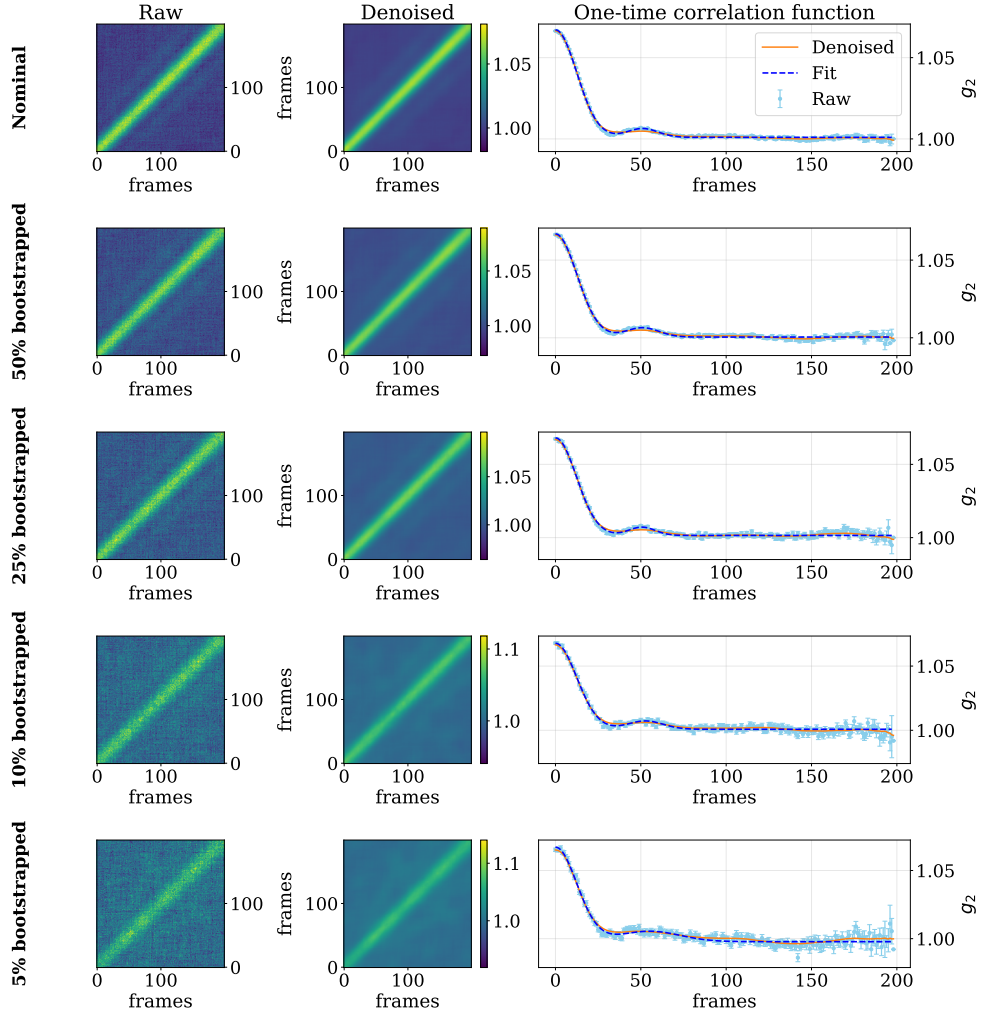


Figure 4: Performance of the FC-DAE in recovering dynamics under progressive data degradation. Each row represents a different bootstrap fraction (Nominal, 50%, 25%, 10%, and 5%), corresponding to increasing noise levels. The first two columns show the raw input and the corresponding FC-DAE-denoised C_2 maps. The third column displays the extracted one-time correlation functions (g_2) for the raw (light blue circles) and denoised (orange line) data, along with a theoretical fit (dashed blue line). The FC-DAE demonstrates robust recovery of the oscillatory component across a wide range of noise levels, with a visible reduction in amplitude only at the most extreme degradation (5% bootstrap), marking the practical limit of information recovery.

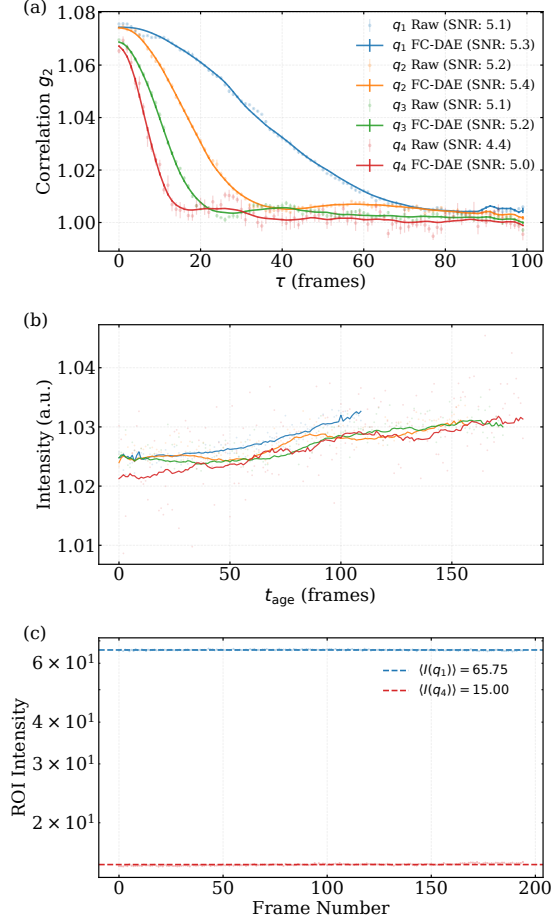


Figure 5: Characterization of correlation functions and intensity stability across varying q -vectors. **(a)** Intensity autocorrelation functions, g_2 , extracted from the central regions of C_2 matrices for q_1, \dots, q_4 . Higher q values correspond to lower photon flux, resulting in a diminished SNR in the raw data, which is subsequently recovered via FC-DAE denoising. **(b)** Diagonal elements of the C_2 matrix at a constant τ time, illustrating temporal intensity fluctuations and denoising performance. **(c)** Average Region of Interest (ROI) intensities for q_1 and q_4 . The disparity in mean counts highlights the challenge of resolving high- q dynamics and demonstrates the potential for significant dose reduction enabled by the denoising algorithm.

Quantitative analysis further demonstrates that the FC-DAE substantially improves the effective SNR of the reconstructed C_2 , enabling reliable extraction of dynamic parameters under photon-limited conditions. Consequently, comparable resolution can be achieved using significantly smaller binning windows, leading to improved temporal resolution for evolving dynamics. The method also extends the accessible experimental parameter space by enabling analysis at larger q values or reduced scattering intensities, where conventional approaches often fail because of poor counting statistics.

Overall, the FC-DAE provides a practical and computationally efficient framework for denoising XPCS correlation data while preserving underlying dynamics. By reducing the need for extensive temporal averaging, the approach enables access rapidly evolving dynamics in XPCS experiments with weak scattering.

10 Data availability

The source code used in this study is available at <https://github.com/NSLS2/Fully-Convolutional-DAE.git>. The training dataset is deposited in Zenodo under DOI: 10.5281/zenodo.20343306.

11 Acknowledgment

We thank Maksim Rakitin, Joshua Lynch, and Andrei Fluerașu for insightful discussions regarding the model and its performance. This research used the CHX and CSX beamlines and resources of the National Synchrotron Light Source II, a U.S. Department of Energy (DOE) Office of Science User Facility operated for the DOE Office of Science by Brookhaven National Laboratory (BNL) under Contract No. DE-SC0012704 and BNL Laboratory Directed Research and Development (LDRD) Project No. 20-038, “Machine Learning for Real-Time Data Fidelity, Healing, and Analysis for Coherent X-ray Synchrotron Data.

References

- [1] Oleg G. Shpyrko. X-ray photon correlation spectroscopy. *Journal of Synchrotron Radiation*, 21(5):1057–1064, 2014.
- [2] Luca Cipelletti, S Manley, RC Ball, and DA Weitz. Universal aging features in the restructuring of fractal colloidal gels. *Physical Review Letters*, 84(10):2275, 2000.
- [3] Andrei Fluerașu, Abdelhadi Moussaïd, Alain Mariot, and George Petekidis. Slow dynamics and aging in colloidal gels studied by x-ray photon correlation spectroscopy. *Physical Review E*, 76(1):010401, 2007.
- [4] Wesley R Burghardt, K Krishnan, Frank S Bates, and Timothy P Lodge. Equilibrium dynamics of a polymer bicontinuous microemulsion. *Macromolecules*, 40(14):5150–5158, 2007.
- [5] OG Shpyrko, ED Isaacs, JM Logan, TF Rosenbaum, G Aeppli, BD Gaulin, JW Kim, Th Vogt, and A Kasman. Direct measurement of antiferromagnetic domain fluctuations. *Nature*, 447(7140):68–71, 2007.
- [6] Anders Madsen, Robert L Leheny, Hongyu Guo, Michael Sprung, and Orsolya Czakkel. Beyond simple exponential correlation functions and equilibrium dynamics in x-ray photon correlation spectroscopy. *New Journal of Physics*, 12(5):055001, may 2010.
- [7] Mark Sutton. A review of x-ray intensity fluctuation spectroscopy. *Comptes Rendus Physique*, 9(5-6):657–667, 2008.
- [8] Rafael C. Gonzalez and Richard E. Woods. *Digital Image Processing*. Pearson/Prentice Hall, Upper Saddle River, NJ, USA, 3rd edition, 2008.
- [9] Salem Saleh Al-amri, N. V. Kalyankar, and S. D. Khamitkar. A comparative study of removal noise from remote sensing image. *arXiv e-prints*, 2010. Mean filter and Gaussian filter among methods compared.

- [10] Tatiana Konstantinova, Lutz Wiegart, Maksim Rakitin, Anthony M. DeGennaro, and Andi M. Barbour. Noise reduction in x-ray photon correlation spectroscopy with convolutional neural networks encoder–decoder models. *Scientific Reports*, 11:14756, 2021.
- [11] Tatiana Konstantinova, Lutz Wiegart, Maksim Rakitin, Anthony M. DeGennaro, and Andi M. Barbour. Machine learning for analysis of speckle dynamics: quantification and outlier detection. *Physical Review Research*, 4(3):033228, 2022.
- [12] Sonja Timmermann, Vladimir Starostin, Anita Girelli, Anastasia Ragulskaya, Hendrik Rahmann, Mario Reiser, Nafisa Begam, Lisa Randolph, Michael Sprung, Fabian Westermeier, Fajun Zhang, Frank Schreiber, and Christian Gutt. Automated matching of two-time x-ray photon correlation maps from phase-separating proteins with cahn–hilliard-type simulations using auto-encoder networks. *Journal of Applied Crystallography*, 55(4):751–757, 2022.
- [13] Christodoulos Kechris, Alexandros Delitzas, Vasileios Matsoukas, and Panagiotis C. Petrantonakis. Removing noise from extracellular neural recordings using fully convolutional denoising autoencoders. In *2021 43rd Annual International Conference of the IEEE Engineering in Medicine & Biology Society (EMBC)*, pages 890–893, 2021.
- [14] Graham Williams and David C. Watts. Non-symmetrical dielectric relaxation behaviour arising from a simple empirical decay function. *Transactions of the Faraday Society*, 66:80–85, 1970.
- [15] Diederik P. Kingma and Jimmy Ba. Adam: A method for stochastic optimization, 2017.
- [16] Zhou Wang, Alan C. Bovik, Hamid R. Sheikh, and Eero P. Simoncelli. Image quality assessment: From error visibility to structural similarity. *IEEE Transactions on Image Processing*, 13(4):600–612, 2004.